Solid-State ^{11}B NMR Studies of Coinage Metal Complexes Containing a Phosphine Substituted Diboraantracene Ligand

Winn Huynh, Jordan W. Taylor, W. Hill Harman* and Matthew P. Conley*

Received 00th January 20xx,
Accepted 00th January 20xx

DOI: 10.1039/x0xx00000x

Transition metal interactions with Lewis acids (M→Z linkages) are fundamentally interesting and practically important. The most common Z-type ligands contain boron, which contains an NMR active ^{11}B nucleus. We measured solid-state $^{11}B\{^1H\}$ NMR spectra of copper, silver, and gold complexes containing a phosphine substituted 9,10-diboraanthracene ligand (B_2P_2))) that contain planar boron centers and weak $M\rightarrow BR_3$ linkages ($[(B_2P_2)M][BAr^F_4]$ (M = Cu (**1**), Ag (**2**), Au (**3**)) characterized by large quadrupolar coupling (C_Q) values (4.4 – 4.7 MHz) and large span (Ω) values (93 – 139 ppm). However, the solid-state $^{11}B\{^1H\}$ NMR spectrum of $K[Au(B_2P_2)]^-$ (**4**), which contains tetrahedral borons, is narrow and characterized by small C_Q and Ω values. DFT analysis of **1** – **4** shows that C_Q and Ω are expected to be large for planar boron environments and small for tetrahedral boron, and that the presence of a $M\rightarrow BR_3$ linkage relates to the reduction in C_Q and ^{11}B NMR shielding properties. Thus solid-state ^{11}B NMR spectroscopy contains valuable information about $M\rightarrow BR_3$ linkages in complexes containing the B_2P_2 ligand.

Introduction

The coordination chemistry of transition metals is dominated by Lewis acid-base interactions in which the transition metal serves as the Lewis acidic partner. However, Lewis pairs in which a transition metal acts as a Lewis base have been known since the late 60s,[1, 2] and over the past two decades, advances in ligand design have resulted in an explosion of complexes featuring Z-type, or Lewis acidic, ligands.[3-5] Although an unsupported $M\rightarrow BR_3$ complex has not yet been structurally authenticated,[6] borane-based chelating ligands feature prominently in this area.[7, 8] This so-called buttressing strategy[3] enables the isolation of complexes where borane coordination might otherwise be labile.[9] High-resolution structural characterization via X-ray diffraction is the gold standard for establishing the presence of a bona fide $M\rightarrow BR_3$ interaction. Transition metal complexes containing tris(methimazolyl)borane,[10-14] phosphinoborane,[15] diphosphinoborane,[16-22] or triphosphinoborane ligands,[23-26] shown in Figure 1a, contain short M–B distances and pyramidalized boron ($\Sigma_{\angle C\text{-}B\text{-}C} < 360°$). However, the "soft" nature of the $M\rightarrow BR_3$ linkage and the geometric constraints imposed by chelation can complicate this analysis. For example, the X-ray structure of a copper complex of a diphosphino borane ligand reported by Bourissou contains four independent molecules, with differences in their Cu–B distances of > 0.1 Å.[27]

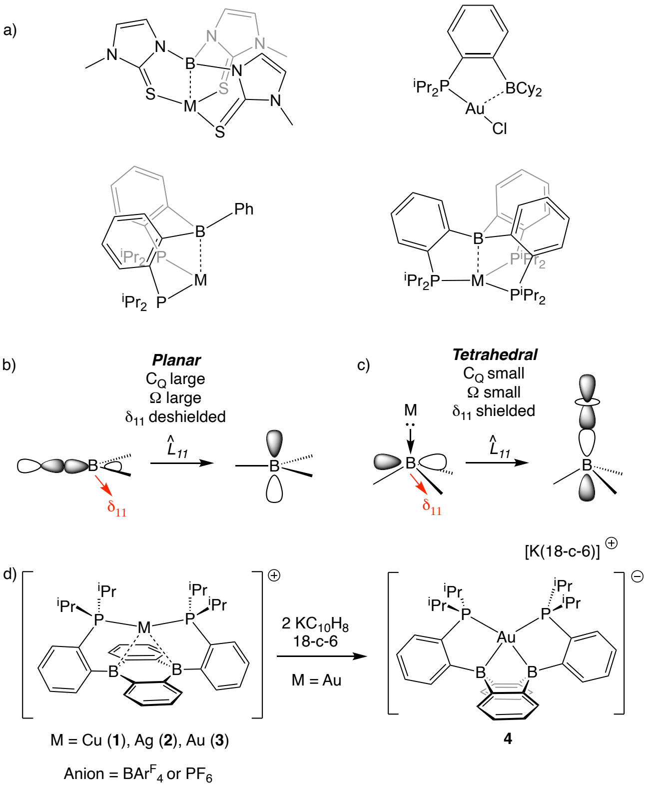

Figure 1. Representative transition metal complexes containing Z-type ligands (a). Predictions of NMR properties for tricoordinate boron (b) and for tetracoordinate boron (c) based on the model proposed in ref 28. Coinage metal complexes of the B_2P_2 ligand and reduction to form the boroauride used for solid-state ^{11}B NMR studies in this work(d).

The NMR active ^{11}B nucleus (8.584×10^7 rad T^{-1} s^{-1}) can serve as a spectroscopic handle for investigating these interactions. In general, the $^{11}B\{^1H\}$ NMR signal in complexes containing a $M\rightarrow BR_3$

---

[a] Department of Chemistry, University of California, Riverside, California 92521, United States

Electronic Supplementary Information (ESI) available: [details of any supplementary information available should be included here]. See DOI: 10.1039/x0xx00000x linkage appear at values associated with tetrahedral boron and are more shielded than the free ligand, similar to trends obtained from $^{11}B\{^1H\}$ NMR chemical shifts in tri- and tetracoordinate boron.[28] The differences in shielding for boron in these different environments is related to the orientation of the Chemical Shift Tensor (CST). The ^{11}B CST is defined by the orientation dependence of the three principal components (δ_{11}, δ_{22}, δ_{33}) that are related to shielding (σ_{ii}) by eq 1. The isotropic chemical shift (δ_{iso}) is the average of the three terms of the CST ($\delta_{iso} = 1/3(\delta_{11} + \delta_{22} + \delta_{33})$), which can be measured in the solid-state. In the Hertzfeld-Berger conventions the CST is described by span ($\Omega = \delta_{11} - \delta_{33}$), the spectral width of the CST, and skew ($\kappa = 3(\delta_{22} - \delta_{iso})/\Omega$).[29]

$$\begin{vmatrix}\delta_{11} & 0 & 0\\ 0 & \delta_{22} & 0\\ 0 & 0 & \delta_{33}\end{vmatrix} = \sigma_{iso}^{ref}\begin{vmatrix}1 & 0 & 0\\ 0 & 1 & 0\\ 0 & 0 & 1\end{vmatrix} - \begin{vmatrix}\sigma_{11} & 0 & 0\\ 0 & \sigma_{22} & 0\\ 0 & 0 & \sigma_{33}\end{vmatrix} \quad (1)$$

Ramsey decomposed shielding contributions into a diamagnetic term (σ^d) that depends on the ground state of the molecule and results in shielding, and a paramagnetic term (σ^p) that results in deshielding. Natural Chemical Shift (NCS) analysis also includes spin-orbit contributions to paramagnetic shielding (σ^{p+SO}, eq 2) chemical shift.[30-32] The magnitude of σ^{p+SO} depends on the coupling between the ground state wavefunction (ϕ_0) and an excited state wavefunction (ϕ_n) through the angular momentum operator ($\hat{L}_{ki}$, where *ki* = element of the shielding tensor, eq 3). Deshielding of a ^{11}B nucleus is related to the magnitude δ_{11}, the most deshielded component of the CST.

$$\sigma = \sigma^d + \sigma^{p+SO} \quad (2)$$

$$\sigma_{ij}^{p+SO} \propto \frac{\langle\varphi_0|\hat{L}_{ki}|\varphi_n\rangle\left\langle\varphi_n\left|\frac{\hat{L}_{kNj}}{r_{kN}^3}\right|\varphi_0\right\rangle}{\Delta E_{n-0}} \quad (3)$$

Figure 1b shows the orientation of δ_{11} in a planar tricoordinate boron. Therefore δ_{11} is expected to be perpendicular to a B–C bonding orbital,[28, 33, 34] and rotation of this orbital about δ_{11} results in the empty p-orbital on boron that is the LUMO of the borane. Because the σ^{p+SO} is inversely proportional to the energies of ϕ_0 and ϕ_n (eq 3), coupling the HOMO and LUMO through the angular momentum operator results in large paramagnetic shielding contributions and, as a consequence, deshielded NMR signals. In tetrahedral $M \rightarrow BR_3$ the δ_{11} axis is oriented in the same direction, but the energy gap between the B–C bonding orbitals (ϕ_0) and $\sigma^*_{M\rightarrow BR3}$ is large, resulting in smaller σ^{p+SO} and shielded NMR signals (Figure 1c).[28] This model is widely applicable to understanding how NMR chemical shifts relate to electronic structures in organic molecules,[35, 36] aryllithium reagents,[37] and organometallic complexes.[31, 38-48] The geometrical perturbation from planar tricoordinate boron to tetrahedral tetracoordinate born shown in Figure 1b-c is also expected to reduce Ω values in experimental solid-state $^{11}B\{^1H\}$ spectra.

Solid-state $^{11}B\{^1H\}$ NMR spectra contain broad powder patterns as a result of interactions between the nuclear electric quadrupole moment, *eQ*, and the electric field gradient (EFG) tensor ***V***, eq 4 ($|V_{33}| \geq |V_{22}| \geq |V_{11}|$).[49-52] The $^{11}B\{^1H\}$ NMR line shape is described by the quadrupolar coupling constant (C_Q, eq 5) and the asymmetry parameter (η, eq 6). The magnitude of C_Q is sensitive to changes in structure. For example, the C_Q of planar Mes_3B (Mes = mesityl) is 4.8 MHz,[33] a larger value than obtained for boronic acids[53] or extended hexagonal boron nitride materials[54] ($C_Q \sim 2.8$ MHz) but a smaller value than the two coordinate Mes_2B^+ borinium ion ($C_Q = 5.4$ MHz).[55] However, these values are far larger than expected for tetrahedral boron environments. Studies of borosilicate glasses showed that tricoordinate boron environments have moderate C_Q values close to those of boronic acids, but framework tetrahedral BO_4 sites have very small C_Q values of ~ 0.4 MHz.[56]

$$\boldsymbol{V} = \begin{vmatrix}V_{11} & 0 & 0\\ 0 & V_{22} & 0\\ 0 & 0 & V_{33}\end{vmatrix} \quad (4)$$

$$C_Q = \frac{eQV_{33}}{h} \quad (5)$$

$$\eta = \frac{V_{11} - V_{22}}{V_{33}} \quad (6)$$

The phosphine substituted 9,10-diboraanthracene ligand (B_2P_2) shown in Figure 1d is a Z-type ligand derived from that reacts with copper, silver, or gold sources to form stable complexes of the form $[(B_2P_2)M][BAr^F_4]$ (Ar^F = 3,5-bistrifluoromethylphenyl).[57, 58] $[(B_2P_2)M][BAr^F_4]$ (M = Cu (**1**), Ag (**2**), Au (**3**)) contain planar boron centers ($\Sigma_{\angle C\text{-}B\text{-}C} \approx 360°$). The solution $^{11}B\{^1H\}$ NMR chemical shifts for **1** – **3** are only slightly perturbed from the ^{11}B NMR chemical shift of the free ligand in solution (δ = 34 ppm in C_6D_6), though the ^{11}B NMR chemical shift should be interpreted with caution due to possible fluxional $R_3P \rightarrow BR_3$ in solution.[59] Reduction of **3** with 2 equiv of potassium napthalenide results in the formation of $[K(18\text{-c-}6)][Au(B_2P_2)]^-$ (**4**) that is best described as a boroauride.[58] The 3c-2e interaction between gold and the two borons in the B_2P_2 ligand stabilize the boroauride, promoting ligand based reactivity of $[Au(B_2P_2)]^-$ towards small molecule substrates.[60-62] **4** shows pronounced pyramidalization at boron ($\Sigma_{C\text{-}B\text{-}C} = 343.8°$) and an shielded $^{11}B\{^1H\}$ NMR chemical shift (δ = 11 ppm in C_6D_6). These data indicate that $[(B_2P_2)M][BAr^F_4]$ contain minimal $M \rightarrow BR_3$ interactions, but $K[Au(B_2P_2)]$ contains a significant $Au \rightarrow BR_3$ interaction. This paper describes the solid-state $^{11}B\{^1H\}$ NMR spectra of **1**–**4** and validates the model shown in Figure 1b-c using DFT and NCS.

Experimental and Computational Methods

1 – **4** were reported previously.[57, 58] Solid state NMR spectra were recorded in 4 mm zirconia rotors packed inside an inert atmosphere glovebox, and acquired on a Bruker 400 Avance III or a Bruker Neo-600 NMR spectrometer. Static $^{11}B\{^1H\}$ NMR spectra were recorded with a Hahn-echo pulse sequence, with full echo detection ($\pi/2 - \tau - \pi$ – acq) and referenced to solid $NaBH_4$ (δ = -42.06 ppm). The $\pi/2$ pulse length for $NaBH_4$ was 6 μsec ($\nu_{rf} = 41.67$ kHz), and a "solid $\pi/2$ pulse" (e.g. 6 μsec/($I + ½$) = 3 μsec for $I = 3/2$ for ^{11}B). Echo delays (τ) were 100 – 250 μsec, and recycle delays were 250 μsec – 1 sec. All analytical simulations of solid-state spectra were performed in Topspin using Sola line shape analysis.

The geometries of all structures were optimized in Gaussian 09[63] using the PBE functional at the 6-31G(d,p) level of theory for H, B, C, and P. Copper, silver, and gold were described with the SDD basis set. The NMR parameters are calculated the Amsterdam Density Functional (ADF) suite,[64] using the GIAO method[65] with the PBE functional, QZ4P basis set on boron, the TZ2P basis set on the metal (Cu, Ag, or Au), and the DZ basis set on all other atoms. Natural Localized Molecular Orbital (NLMO)[66] contributions to shielding were also calculated at this level of theory, with scalar relativistic ZORA included in this analysis.[67] This analysis in ADF gives shielding (σ) as the sum of diamagnetic shielding (σ^d) and of the full paramagnetic shielding term (σ^{p+so}), which is the sum of paramagnetic shielding and spin-orbit contributions.

Results and Discussion

NMR Properties and DFT Studies of the B_2P_2 Ligand

The static $^{11}B\{^1H\}$ NMR spectrum of the B_2P_2 ligand acquired at 9.4 T is shown in Figure 2, and the NMR data extracted from this spectrum are given in Table 1. Complementary measurements at 14.1 T are shown in the Supporting Information (Figure S1). This spectrum contains one broad signal at 63 ppm and one narrow signal at 9 ppm. By contrast, the room temperature C_6D_6 solution spectrum contains a single signal at 34 ppm, near the average of the two chemical shifts observed in the solid state. The presence of two signals in the solid-state $^{11}B\{^1H\}$ NMR spectrum of B_2P_2 at the average chemical shift observed in solution suggests that $R_3P \rightarrow BR_3$ interactions are present in the solid-state and are fluxional on the NMR timescale in solution, which is was previously observed in a tri-phosphinoborane ligand.[59] The ^{11}B NMR parameters are consistent with this scenario because the deshielded ^{11}B NMR signal at 63 ppm contains a larger C_Q of 4.8 MHz and larger Ω of 77 ppm, suggesting a planar tri-coordinate boron, than the shielded signal at 9 ppm (C_Q = 2.9 MHz; Ω = 35 ppm), suggesting a distorted tetrahedral boron.

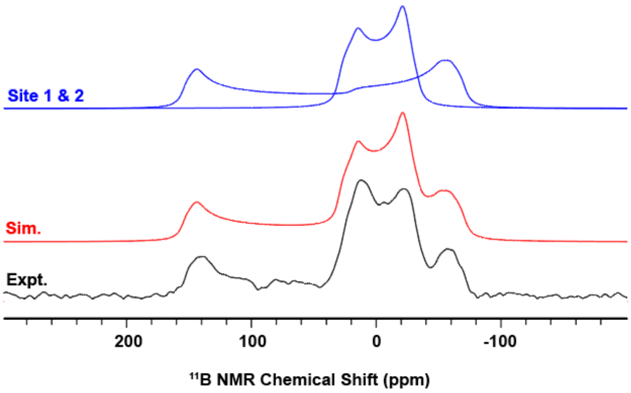

Figure 2. Static $^{11}B\{^1H\}$ NMR spectrum of B_2P_2 acquired at 9.4 T. Experimental spectra are shown in black and simulated spectra are shown in red. The two simulated boron sites in B_2P_2 are shown in blue above the red simulated spectrum.

Table 1. $^{11}B\{^1H\}$ NMR data extracted from solid-state NMR measurements of $\mathbf{B_2P_2}$.[a]

	Site-1	Site-2
δ (ppm)[b]	63	9
C_Q (MHz)	4.8	2.9
η	0.05	0.02
Ω (ppm)	77	35
κ	0.6	-0.2
δ_{11}	93	28
δ_{22}	78	7
δ_{33}	17	-7
α	122	15
β	4	175
γ	272	200

[a] – data shown in the table are averages from simulations from data acquired at 9.4 T and 14.1 T, the simulated data from both field strengths are given in the Supporting Information (Table S2-3); [b] – ^{11}B NMR chemical shift in C_6D_6 solution is 34 ppm, see ref 57.

The geometries of B_2P_2 were optimized using DFT (PBE/6-31G(d,p)) in *syn-* and *anti*-conformations, Figure 3. The relative energies of these three geometries are *syn*-B_2P_2 (0.0 kcal mol^{-1}, Figure 3a), *anti*-B_2P_2 shown in Figure 3b (3.6 kcal mol^{-1}), and the *anti*-B_2P_2 showns in Figure 3c (3.0 kcal mol^{-1}). The B–P distance in the *syn*-B_2P_2 isomer is 2.80 Å, while the B–P distances in the *anti*-B_2P_2 isomer shown in Figure 4b are 3.01 and 3.08 Å. These values are significantly longer than the sum of covalent radii for boron and phosphorus (1.91 Å). In addition, the $\Sigma_{\angle C\text{-}B\text{-}C}$ is ~360° in these conformers, indicating that boron is planar and that significant $R_3P \rightarrow BR_3$ interactions are not present. The *anti*-conformer shown in Figure 4c contains one planar boron ($\Sigma_{\angle C\text{-}B\text{-}C}$ = 360°) with a long B–P distance (3.06 Å) and one distorted tetrahedral boron ($\Sigma_{\angle C\text{-}B\text{-}C}$ = 354°) containing a short B–P distance (2.25 Å), consistent with a $R_3P \rightarrow BR_3$ interaction. This conformer is 0.61 kcal mol^{-1} more stable than the *anti*-conformer lacking a $R_3P \rightarrow BR_3$ interaction at this level of theory.

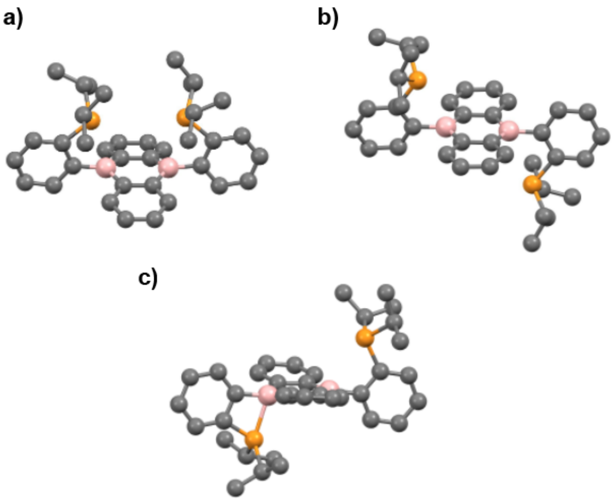

Figure 3. Calculated structures of *syn*-B_2P_2 (a), *anti*-B_2P_2 lacking a $R_3P \rightarrow BR_3$ interaction (b), and *anti*-B_2P_2 containing a $R_3P \rightarrow BR_3$ interaction (c). Refer to the Supporting Information (Table S4) for relevant bond distances and angles.

^{11}B NMR parameters for *syn*-B_2P_2 and the two *anti*-B_2P_2 were calculated at the PBE/QZ4P(B)/DZ(P,C,H) level of theory, and are given in Table 2. The planar boron environment in each is characterized by large C_Q values (4.7 – 4.9 MHz) and large Ω values (85 – 105 ppm). The distorted tetrahedral boron site in the *anti*-conformer containing a $R_3P \rightarrow BR_3$ interaction has a significantly smaller C_Q of 2.8 MHz and Ω of 33 ppm. The calculated ^{11}B NMR properties of the *anti*-conformer containing a $R_3P \rightarrow BR_3$ closely match those obtained experimentally. The data for the B_2P_2 is an important benchmark for the studies of **1** – **4**, and supports the expectations described in Figure 1c that planar boron sites are characterized by large C_Q and Ω values and that tetrahedral boron sites are characterized by small C_Q and Ω values in this ligand. These data also show that solid-state ^{11}B NMR properties are very sensitive to fairly minor structural distortions at boron.

Table 2. Calculated $^{11}B\{^1H\}$ NMR data for the structures of $\mathbf{B_2P_2}$ shown in Figure 3.[a]

	syn- B_2P_2	*anti-* B_2P_2-**1**	*anti-* B_2P_2-**2**[b]	*anti-* B_2P_2-**2**[c]
δ (ppm)	47	56	55	9
C_Q (MHz)	4.7	4.9	4.77	3.26
η	0.07	0.06	0.07	0.13
Ω (ppm)	96	105	102	38
κ	0.2	0.2	0.24	0.22
δ_{11}	92	105	102	26
δ_{22}	53	63	63	12
δ_{33}	-4	0	0	-11
α	90	80	90	85
β	163	4	163	12
γ	270	275	281	272

[a] – Individual boron sites have slightly different NMR parameters, where they differ averages are given; [b] – values for the planar boron for the *anti*-B_2P_2 shown in Figure 3c; [c] – values for the distorted tetrahedral boron for the *anti*-B_2P_2 shown in Figure 3c.

NMR Properties of 1 – 4

The solid-state $^{11}B\{^1H\}$ NMR spectra for **1** and **2** resemble those of **3** and are provided in the Supporting Information (Figure S1). The solid-state $^{11}B\{^1H\}$ NMR spectrum of **3** acquired at 14.1 T is shown in Figure 5a and contains two ^{11}B resonances, one broad signal at 51 ppm from the nearly planar borons present in the B_2P_2 ligand framework and a second narrow signal from the tetrahedral $[\mathrm{BAr^F}_4]$ anion at –11ppm. Similar features are obtained at 9.4 T (see Figure S1). This result is consistent with equivalent boron environments from the B_2P_2 fragment in **3** from X-ray diffraction studies of **3**.[58]

The ^{11}B NMR properties extracted from the simulations at both magnetic field strengths for **1**–**3** are given in Table 3. Critically, the broad signals observed in the solid-state for the diboraanthracene borons in **1**–**3** occur at chemical shifts that differ substantially from those measuremed in CD_3CN solution. The ^{11}B NMR parameters for **1**–**3** show that the borons in the B_2P_2 ligand have isotropic chemical shifts significantly deshielded of those obtained in CD_3CN solution and increase in the order **1** < **2** < **3**. We attribute this discrepancy to rapid, reversible interactions of the CD_3CN solvent with the B_2P_2 boron sites. Although we had observed some solvent dependence of the ^{11}B chemical shifts in these cations, the solid-state values are uniformly higher than any solution values we have determined. This phenomenon highlights the utility of solid-state ^{11}B NMR in this role, as the solution-derived chemical shift values do not accurately report on the intrinsic $M \rightarrow BR_3$ interaction.

The large C_Q values (4.4 – 4.7 MHz) extracted from the $^{11}B\{^1H\}$ NMR spectra for **1** – **3** are consistent with planar boron sites in the B_2P_2 fragment and suggest minimal interaction between the coinage metal cation and boron. Supporting this conjecture, the Ω values across this series increase with respect to the planar boron present in free B_2P_2 ($\Omega = 77$ ppm), increasing from 93 ppm (Cu) to 102 ppm (Ag) to 139 ppm (Au). The increase in Ω is related to the deshielding of the δ_{11} component of the CST in **1**–**3**, suggesting a common origin the of the chemical shift tensor in these compounds.

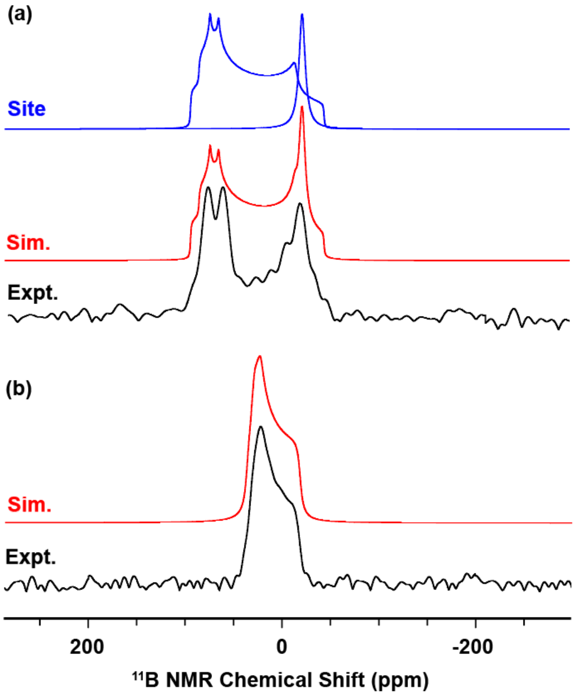

Figure 4. Static $^{11}B\{^1H\}$ NMR spectrum of **3** (a) and **4** (b) acquired at 14.1 T. Experimental spectra are shown in black and simulated spectra are shown in red. The two simulated boron sites in **3** are shown in blue above the red simulated spectrum.

Table 3. $^{11}B\{^1H\}$ NMR data extracted from solid-state NMR measurements of **1** – **4**.[a]

	1	**2**	**3**	**4**
δ (ppm)[b]	27[c]	29[d]	32[c]	11[e]
δ (ppm)[f]	51[g]	55	66	15
C_Q (MHz)	4.4	4.4	4.7	1.5
η	0.2	0.04	0.03	0.2
Ω (ppm)	93	105	139	56
κ	0.3	0.3	0.2	0.7
δ_{11}	93	102	131	36
δ_{22}	60	66	75	28
δ_{33}	-0.2	-3	-8	-20
α	180	275	178	60
β	0	180	126	90
γ	90	91	40	180

[a] – solid-state data shown in the table are averages from simulations from spectra acquired at 9.4 T and 14.1 T, the simulated data from both field strengths are given in the Supporting Information; [b] – ^{11}B NMR chemical shift in solution, see ref 10; [c] – measured as the $[PF_6]^-$ salt in CD_3CN; [d] – measured as the $[\mathrm{BAr^F}_4]^-$ salt in CD_3CN; [e] — measured in C_6D_6; [f] – ^{11}B NMR chemical shift from solid-state measurements; [g] – $[PF_6]^-$ salt.

The static solid-state $^{11}B\{^1H\}$ NMR spectrum of **4** is shown in Figure 4b, and differs significantly from **1** – **3**. This spectrum contains one signal at 15 ppm with a small C_Q of 1.5 MHz and a small Ω of 56 ppm. These values are significantly smaller than those obtained for **1** – **3**, and are consistent with the significant $M \rightarrow BR_3$ interaction in **4** that is expected from diffraction studies. These data also indicate that the origin of the NMR properties of **4** are different than those for **1** – **3**.

DFT Studies of **1 – 4**

The geometries of **1**–**4** were optimized using DFT (PBE/SDD(metal)/6-31G(d,p)). This level of theory gives M–B and M–P bond distances as well as B–M–P and C–B–C bond angles that agree well with those obtained experimentally (Table S5 – S8). NMR parameters were calculated at the PBE/QZ4P(B)/TZ2P(metal)/DZ(P,C,H) level of theory and are given in Table 4. The calculated isotropic ^{11}B NMR chemical shifts are shifted ~10 ppm more shielded than experimental values obtained in the solid-state. However, the C_Q and Ω values agree well with the trends obtained experimentally. **1** – **3** are predicted to have C_Q between 4.3 and 4.6 MHz and Ω between 109 and 119 ppm, and followed the experimental trends such that Ω increases in the order **1** < **2** < **3**. Similar to the experimental data, the increase in Ω is related to deshielding of the δ_{11} component of the chemical shift tensor in the order **1** < **2** < **3**. This level of theory also reproduces the C_Q and Ω for **4**, and is consistent with the view that the NMR properties in **4** are distinct from **1** – **3**.

The isotropic ^{11}B NMR chemical shifts obtained from experimentally from solid-state measurements computationally are more deshielded than those obtained in CD_3CN solution. We also calculated the mono- and bis-MeCN adducts of **1** at the same level of theory. As expected, MeCN binds to the boron(s) in **1**. Coordination of one MeCN to **1** is 2.7 kcal mol^{-1} less stable than separated reactants and results in one shielded (δ = -13 ppm, C_Q = 2.6 MHz, and Ω = 26 ppm) and one deshielded (δ = 37 ppm, C_Q = 3.9 MHz, and Ω = 96 ppm) ^{11}B NMR signal. Coordination of two MeCN to **2** is 15.9 kcal mol^{-1} less stable than separated reactants and results in two shielded ^{11}B NMR signals (δ = -13ppm, C_Q = 2.5 MHz, and Ω = 23 ppm).

Table 4. Calculated ^{11}B{^{1}H} NMR parameters for **1** – **4**

	1	**2**	**3**	**4**
δ (ppm)	41	47	49	5
C_Q (MHz)	4.3	4.5	4.6	1.8
η	0.02	0.03	0.05	0.2
Ω (ppm)	109	116	119	56
κ	0.7	0.1	0.1	0.2
δ_{11}	94	103	106	31
δ_{22}	44	51	53	9
δ_{33}	-15	-13	-13	-25
α	118	255	278	88
β	4	151	148	89
γ	85	90	89	102

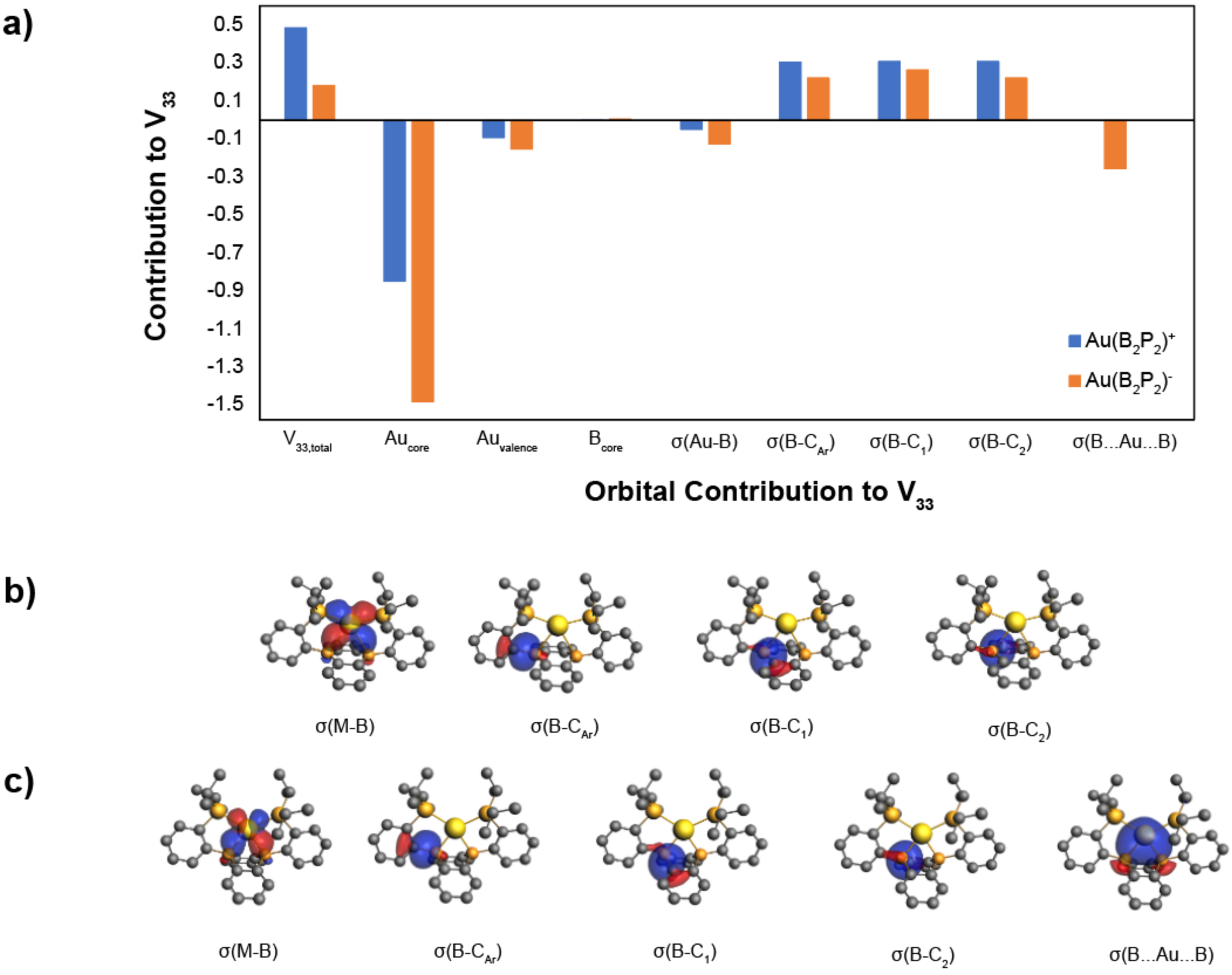

Figure 5. NLMO contributions to V_{33} in **3** (blue) and **4** (orange, a); plots of NLMOs for **3** (b) and **4** (c); isovalue = 0.03.

The discussion below describes the origin of the differences in C_Q and Ω in these compounds, but largely focuses on **3** and **4**. **1** and **2** follow similar trends as **3**, and complementary data for these compounds are given in the Supporting Information. The V_{33} component of the EFG tensor in **3** is oriented perpendicular to the plane defined by the three B–C bonds while the V_{33} component of the EFG tensor in **4** is oriented along the B–Au axis (Figure S3). Figure 5 shows the contributions of Natural Localized Molecular Orbitals (NLMOs) to V_{33} for **3** and **4**.[49, 51, 68, 69] The largest differences in NLMO contribution to V_{33} in **1** – **4** are metal core orbitals, all of which reduce V_{33} significantly in the order $Cu^+ < Ag^+ < Au^+ < Au^-$ (Figure S4). This decrease in V_{33} is due to Sternheimer shielding, which increases down the Group 11 period as the metal becomes more polarizable. The short Au–B distances in **4** result in larger negative V_{33} contributions from Au core orbitals than in **3**. In both **3** and **4** all three $\sigma_{B\text{–}C}$ orbitals contribute to V_{33}, with slightly larger contributions for **3** (Figure 6d – e). The NLMOs describing the bonding between gold and boron for both **3** and **4** reduce V_{33}. The $\sigma_{Au\text{-}B}$ NLMO is a modestly more negative contributor to V_{33} in **4** than in **3**, but in both cases this orbital is significantly more localized on gold than on boron. The 3c-2e NLMO that describes the boroauride in **4** reduces V_{33} significantly. These results show that $Au\rightarrow BR_3$ bonding results in a small C_Q values in **4** due to the greater contribution of core orbitals to V_{33} and the pronounced 3c-2e interaction between Au and the two borons in the B_2P_2 ligand in **4**.

The CST for **3** and **4** are shown in Figure 7a – b. The CST of **3** is more anisotropic than **4**, as expected from the calculated NMR parameters in Table 4. The δ_{11} component of the CST, which is responsible for the difference in shielding in this series, is oriented perpendicular to the $B\text{–}C_{aryl}$ bond in both **3** and **4**, and lies roughly along the plane defined by the diboranthacene ring (Figure 6c). Analysis of NLMO contributions to the CST show that the $B\text{–}C_{aryl}$ bond is the largest contributor to σ^{p+SO} in **3** and **4** (Figure 6d – e).

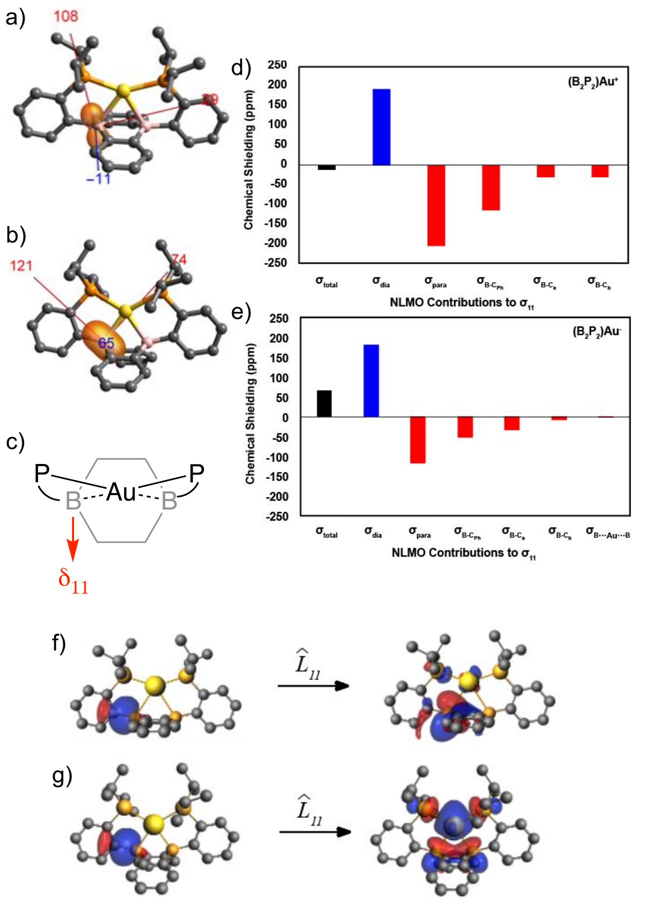

Figure 6. TensorView[70] plots of the Shielding tensor of **3** (a) and **4** (b). The numbers in these plots are the magnitudes of the three components of the CST. A Newman type projection of showing that the orientation of δ_{11} in **3** and **4** is the same in both compounds (c). NLMO decomposition of σ_{11} for **3** (d) and **4** (e). NLMOs that contribute to σ_{11} for **3** (f) and **4** (g). NLMOs are displayed at iso value = 0.03.

Though the alignment of the δ_{11} component of the CST is similar in **3** and **4**, the magnitude of shielding between **3** and **4** is quite different. This is a result of the orbitals coupled to the $\sigma_{B\text{–}Caryl}$ NLMO through the angular momentum operator (eq 3). In **3** rotation of the $\sigma_{B\text{–}Caryl}$ orbital by 90° about the δ_{11} axis results in the π^* of the $d\pi_{Au}\rightarrow p_B$ (Figure 6f). In **4**, rotation of the $\sigma_{B\text{–}Caryl}$ about the δ_{11} axis results in the 3c-2e σ^* orbital shown in Figure 6g. These results show that (de)shielding in the ^{11}B NMR chemical shift is also related to NLMOs involved in $Au\rightarrow BR_3$ interactions.

The greater deshielding in **3** compared to **4** can be rationalized by the qualitative molecular orbital diagram shown in Figure 7. In **3** the $\sigma_{B\text{–}Caryl}$ orbital and the π^* of the $d\pi_{Au}\rightarrow p_B$ interaction are orthogonal, similar to the planar boron model shown in Figure 2. This results in a small ΔE term in eq 3, and a large σ^{p+SO}. Adding two electrons to **3** populates the non-bonding s-orbital in $5d^{10}$ Au^+ to form the $5d^{10}s^2$ Au^- in **4**. Though the $\sigma_{B\text{–}C_{aryl}}$ orbital also contributes to deshielding in **4**, coupling to the 3c-2e σ* orbital has a larger ΔE than encountered for **3**.

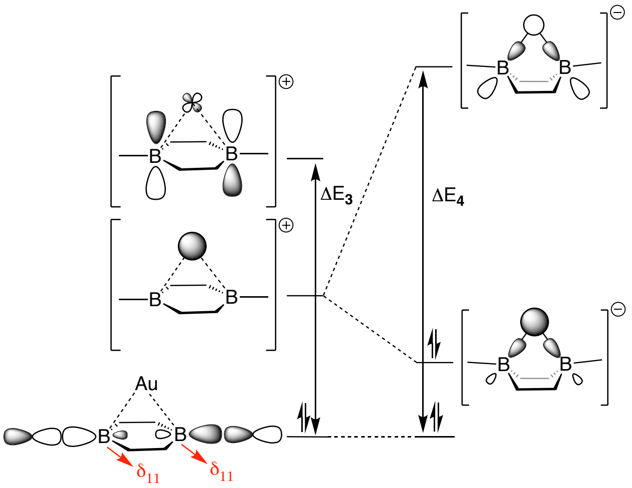

Figure 7. Qualitative molecular orbital diagram showing how ΔE (σ^{p+SO}) changes by adding two electrons to **3** (right diagram) to form **4** (left diagram).

The difference in C_Q and shielding in **3** and **4** is related, at least in part, to the strength of the $Au\rightarrow BR_3$ interaction. As mentioned above, the NLMO that describes the $d\pi_{Au}\rightarrow p_B$ interaction in **3** (Figure 5a) is localized on gold [93% Au (100% d); 2 % per B (3%s, 97% p)]. The second order perturbation energy for delocalization of $d\pi_{Au}\rightarrow p_B$ at this level of theory is only 3.7 kcal mol^{-1} per boron, indicating that the $Au\rightarrow BR_3$ interaction in **3** is rather weak. The $Cu\rightarrow BR_3$ in **1** and the $Ag\rightarrow BR_3$ interactions in **1** and **2** are slightly weaker (2.8 kcal mol^{-1}(Cu) and 3.4 kcal mol^{-1} (Ag), respectively). In **4** this NLMO is also localized on gold [87% Au (100% d); 6% per B (16%s, 84% p)], and does not contribute to shielding but does reduce C_Q. The $d\pi_{Au}\rightarrow p_B$ in **4** is significantly stronger (14.8 kcal mol^{-1} per boron) in **4** than in **3**, but modest in comparison to other $M\rightarrow BR_3$ interactions.[3] However, the 3c-2e boroauride interaction is more evenly populated between Au and B [33% Au (97% s, 3%d); 28%B (13%s, 87%p); 28%B (13%s, 87%p)] and reduces both C_Q and σ^{p+SO}.

Conclusions

In **1** – **3** the planar boron and long M•••B contacts result in large C_Q and Ω values. DFT calculations show that **1** – **3** contain weak $M\rightarrow BR_3$ Z-type bonding, and though the $M\rightarrow BR_3$ donation is minimal there are slight reductions in C_Q and shielded $^{11}B\{^1H\}$ NMR chemical shift with respect to the planar boron in the B_2P_2 ligand. Addition of two electrons to **3** generates the boroauride **4**. Similar to **1** – **3**, the $Au\rightarrow BR_3$ interactions in **4** influence C_Q and Ω, though the stronger $Au\rightarrow BR_3$ donation ($d\pi_{Au}\rightarrow p_B = 14.8$ kcal mol^{-1}) and the 3c-2e B–Au–B interaction results in small C_Q values and a narrow Ω that are characteristic of the tetrahedral geometry at boron that are indicative of significant $Au\rightarrow BR_3$ interactions. The difference in ^{11}B NMR properties between **1** – **3** and **4** validate models for ^{11}B NMR chemical shift analysis widely used in the field of $M\rightarrow BR_3$ complexes.[28] These studies also show that C_Q is very sensitive to the presence or absence of $M\rightarrow BR_3$ linkages in **1** – **4**. C_Q is usually not reported for compounds containing $M\rightarrow BR_3$ linkages because $^{11}B\{^1H\}$ NMR measurements are acquired in solution. In situations where ambiguities in assigning $M\rightarrow BR_3$ linkages persist, and solid-state NMR measurements are not possible, analysis of the $^{11}B\{^1H\}$ NMR lineshape from solution measurements can also give a fairly accurate measurement of C_Q,[71-75] which could provide evidence for the presence or absence of a $M\rightarrow BR_3$ linkage.

Author Contributions

M. P. C. and W. H. H. conceptualized the study. W. H. and J. T. acquired and curated data. W. H. acquired and analyzed DFT data. All authors contributed to the preparation of this manuscript.

Conflicts of interest

There are no conflicts to declare.

Acknowledgements

M. P. C. and W. H. H. are members of the UCR Center for Catalysis. We thank Prof. Leonard Mueller for discussions and access to his group's 9.4 T NMR spectrometer. The solid-state NMR measurements at 14.1 T were recorded on an instrument supported by the National Science Foundation (CHE-1626673). This work was supported by the University of California, Riverside and in part by the National Science Foundation (CHE-2101582 to MPC; CHE-1752876 to WHH).

Notes and references

1. K. W. Muir and J. A. Ibers, *Inorg. Chem.*, 1969, **8**, 1921-1928.
2. J. M. Burlitch, M. E. Leonowicz, R. B. Petersen and R. E. Hughes, *Inorg. Chem.*, 1979, **18**, 1097-1105.
3. A. Amgoune and D. Bourissou, *Chem. Commun.*, 2011, **47**, 859-871.
4. D. You and F. P. Gabbaï, *Trends in Chemistry*, 2019, **1**, 485-496.
5. G. Bouhadir and D. Bourissou, in *The Chemical Bond III: 100 years old and getting stronger*, ed. D. M. P. Mingos, Springer International Publishing, Cham, 2017, DOI: 10.1007/430_2015_201, pp. 141-201.
6. H. Braunschweig, *Angew. Chem., Int. Ed.*, 1998, **37**, 1786-1801.
7. H. Braunschweig and R. D. Dewhurst, *Dalton Trans.*, 2011, **40**, 549-558.
8. H. Braunschweig, R. D. Dewhurst and A. Schneider, *Chem. Rev.*, 2010, **110**, 3924-3957.
9. B. R. Barnett, C. E. Moore, A. L. Rheingold and J. S. Figueroa, *J. Am. Chem. Soc.*, 2014, **136**, 10262-10265.
10. A. F. Hill, G. R. Owen, A. J. P. White and D. J. Williams, *Angew. Chem., Int. Ed.*, 1999, **38**, 2759-2761.
11. J. S. Figueroa, J. G. Melnick and G. Parkin, *Inorg. Chem.*, 2006, **45**, 7056-7058.
12. V. K. Landry, J. G. Melnick, D. Buccella, K. Pang, J. C. Ulichny and G. Parkin, *Inorg. Chem.*, 2006, **45**, 2588-2597.
13. K. Pang, J. M. Tanski and G. Parkin, *Chem. Commun.*, 2008, DOI: 10.1039/B714466K, 1008-1010.
14. K. Pang, S. M. Quan and G. Parkin, *Chem. Commun.*, 2006, DOI: 10.1039/B611654J, 5015-5017.

15. S. Bontemps, G. Bouhadir, K. Miqueu and D. Bourissou, *J. Am. Chem. Soc.*, 2006, **128**, 12056-12057.
16. S. Bontemps, H. Gornitzka, G. Bouhadir, K. Miqueu and D. Bourissou, *Angew. Chem., Int. Ed.*, 2006, **45**, 1611-1614.
17. S. Bontemps, M. Sircoglou, G. Bouhadir, H. Puschmann, J. A. K. Howard, P. W. Dyer, K. Miqueu and D. Bourissou, *Chemistry – A European Journal*, 2008, **14**, 731-740.
18. M. Sircoglou, S. Bontemps, M. Mercy, N. Saffon, M. Takahashi, G. Bouhadir, L. Maron and D. Bourissou, *Angew. Chem., Int. Ed.*, 2007, **46**, 8583-8586.
19. P. Steinhoff and M. E. Tauchert, *Beilstein J. Org. Chem.*, 2016, **12**, 1573-1576.
20. W. H. Harman and J. C. Peters, *J. Am. Chem. Soc.*, 2012, **134**, 5080-5082.
21. D. L. M. Suess and J. C. Peters, *J. Am. Chem. Soc.*, 2013, **135**, 12580-12583.
22. M. A. Nesbit, D. L. M. Suess and J. C. Peters, *Organometallics*, 2015, **34**, 4741-4752.
23. M. Sircoglou, S. Bontemps, G. Bouhadir, N. Saffon, K. Miqueu, W. Gu, M. Mercy, C.-H. Chen, B. M. Foxman, L. Maron, O. V. Ozerov and D. Bourissou, *J. Am. Chem. Soc.*, 2008, **130**, 16729-16738.
24. S. Bontemps, G. Bouhadir, W. Gu, M. Mercy, C.-H. Chen, B. M. Foxman, L. Maron, O. V. Ozerov and D. Bourissou, *Angew. Chem., Int. Ed.*, 2008, **47**, 1481-1484.
25. M.-E. Moret and J. C. Peters, *Angew. Chem., Int. Ed.*, 2011, **50**, 2063-2067.
26. D. L. M. Suess, C. Tsay and J. C. Peters, *J. Am. Chem. Soc.*, 2012, **134**, 14158-14164.
27. M. Sircoglou, S. Bontemps, M. Mercy, K. Miqueu, S. Ladeira, N. Saffon, L. Maron, G. Bouhadir and D. Bourissou, *Inorg. Chem.*, 2010, **49**, 3983-3990.
28. S. Hermanek, *Chem. Rev.*, 1992, **92**, 325-362.
29. J. Herzfeld and A. E. Berger, *J. Chem. Phys.*, 1980, **73**, 6021-6030.
30. J. A. Bohmann, F. Weinhold and T. C. Farrar, *J. Chem. Phys.*, 1997, **107**, 1173-1184.
31. A. Jochen and Z. Shaohui, *Magn. Reson. Chem.*, 2008, **46**, S45-S55.
32. F. Aquino, B. Pritchard and J. Autschbach, *J. Chem. Theory Comput.*, 2012, **8**, 598-609.
33. D. L. Bryce, R. E. Wasylishen and M. Gee, *J. Phys. Chem. A*, 2001, **105**, 3633-3640.
34. W. Huynh and M. P. Conley, *Dalton Trans.*, 2020, **49**, 16453-16463.
35. K. B. Wiberg, J. D. Hammer, K. W. Zilm and J. R. Cheeseman, *J. Org. Chem.*, 1999, **64**, 6394-6400.
36. R. V. Viesser, L. C. Ducati, C. F. Tormena and J. Autschbach, *Chem. Sci.*, 2017, **8**, 6570-6576.
37. S. Berger, U. Fleischer, C. Geletneky and J. C. W. Lohrenz, *Chem. Ber.*, 1995, **128**, 1183-1186.
38. B. Pinter, K. T. Smith, M. Kamitani, E. M. Zolnhofer, B. L. Tran, S. Fortier, M. Pink, G. Wu, B. C. Manor, K. Meyer, M.-H. Baik and D. J. Mindiola, *J. Am. Chem. Soc.*, 2015, **137**, 15247-15261.
39. C. P. Gordon, K. Yamamoto, W. C. Liao, F. Allouche, R. A. Andersen, C. Coperet, C. Raynaud and O. Eisenstein, *ACS Cent. Sci.*, 2017, **3**, 759-768.
40. K. Yamamoto, C. P. Gordon, W. C. Liao, C. Coperet, C. Raynaud and O. Eisenstein, *Angew. Chem., Int. Ed.*, 2017, **56**, 10127-10131.
41. C. P. Gordon, K. Yamamoto, K. Searles, S. Shirase, R. A. Andersen, O. Eisenstein and C. Coperet, *Chem. Sci.*, 2018, **9**, 1912-1918.
42. D. P. Estes, C. P. Gordon, A. Fedorov, W. C. Liao, H. Ehrhorn, C. Bittner, M. L. Zier, D. Bockfeld, K. W. Chan, O. Eisenstein, C. Raynaud, M. Tamm and C. Coperet, *J. Am. Chem. Soc.*, 2017, **139**, 17597-17607.
43. S. Halbert, C. Coperet, C. Raynaud and O. Eisenstein, *J. Am. Chem. Soc.*, 2016, **138**, 2261-2272.
44. D. B. Culver, W. Huynh, H. Tafazolian, T.-C. Ong and M. P. Conley, *Angew. Chem., Int. Ed.*, 2018, **57**, 9520-9523.
45. C. P. Gordon and C. Copéret, *Angew. Chem., Int. Ed.*, 2020, **59**, 7035-7041.
46. C. P. Gordon, C. Raynaud, R. A. Andersen, C. Copéret and O. Eisenstein, *Acc. Chem. Res.*, 2019, **52**, 2278-2289.
47. G. Wu, D. Rovnyak, M. J. A. Johnson, N. C. Zanetti, D. G. Musaev, K. Morokuma, R. R. Schrock, R. G. Griffin and C. C. Cummins, *J. Am. Chem. Soc.*, 1996, **118**, 10654-10655.
48. C. P. Gordon, L. Lätsch and C. Copéret, *The Journal of Physical Chemistry Letters*, 2021, **12**, 2072-2085.
49. J. Autschbach, S. Zheng and R. W. Schurko, *Conc. Mag. Res. A*, 2010, **36A**, 84-126.
50. S. E. Ashbrook and S. Sneddon, *J. Am. Chem. Soc.*, 2014, **136**, 15440-15456.
51. S. Monika and A. Jochen, *Chemistry – A European Journal*, 2013, **19**, 12018-12033.
52. Y.-T. Angel Wong and D. L. Bryce, in *Annu. Rep. NMR Spectrosc.*, ed. G. A. Webb, Academic Press, 2018, vol. 93, pp. 213-279.
53. J. W. E. Weiss and D. L. Bryce, *J. Phys. Chem. A*, 2010, **114**, 5119-5131.
54. A. M. Love, B. Thomas, S. E. Specht, M. P. Hanrahan, J. M. Venegas, S. P. Burt, J. T. Grant, M. C. Cendejas, W. P. McDermott, A. J. Rossini and I. Hermans, *J. Am. Chem. Soc.*, 2019, **141**, 182-190.
55. A. E. Alain, Y. Shoji, T. Fukushima and D. L. Bryce, *Inorg. Chem.*, 2015, **54**, 11889-11896.
56. G. L. Turner, K. A. Smith, R. J. Kirkpatrick and E. Oldfield, *Journal of Magnetic Resonance (1969)*, 1986, **67**, 544-550.
57. J. W. Taylor, A. McSkimming, M.-E. Moret and W. H. Harman, *Inorg. Chem.*, 2018, **57**, 15406-15413.
58. J. W. Taylor, A. McSkimming, M.-E. Moret and W. H. Harman, *Angew. Chem., Int. Ed.*, 2017, **56**, 10413-10417.
59. S. Bontemps, G. Bouhadir, P. W. Dyer, K. Miqueu and D. Bourissou, *Inorg. Chem.*, 2007, **46**, 5149-5151.
60. J. W. Taylor, A. McSkimming, L. A. Essex and W. H. Harman, *Chem. Sci.*, 2019, **10**, 9084-9090.
61. J. W. Taylor and W. H. Harman, *Chem. Commun.*, 2020, **56**, 4480-4483.
62. J. W. Taylor and W. H. Harman, *Chem. Commun.*, 2020, **56**, 13804-13807.
63. G. W. T. M. J. Frisch, H. B. Schlegel, G. E. Scuseria, M. A. Robb, J. R. Cheeseman, G. Scalmani, V. Barone, G. A. Petersson, H. Nakatsuji, X. Li, M. Caricato, A. Marenich, J. Bloino, B. G. Janesko, R. Gomperts, B. Mennucci, H. P. Hratchian, J. V. Ortiz, A. F. Izmaylov, J. L. Sonnenberg, D. Williams-Young, F. Ding, F. Lipparini, F. Egidi, J. Goings, B. Peng, A. Petrone, T. Henderson, D. Ranasinghe, V. G. Zakrzewski, J. Gao, N. Rega, G. Zheng, W. Liang, M. Hada, M. Ehara, K. Toyota, R. Fukuda, J. Hasegawa, M. Ishida, T. Nakajima, Y. Honda, O. Kitao, H. Nakai, T. Vreven, K. Throssell, J. A. Montgomery Jr., J. E. Peralta, F. Ogliaro, M.

Bearpark, J. J. Heyd, E. Brothers, K. N. Kudin, V. N. Staroverov, T. Keith, R. Kobayashi, J. Normand, K. Raghavachari, A. Rendell, J. C. Burant, S. S. Iyengar, J. Tomasi, M. Cossi, J. M. Millam, M. Klene, C. Adamo, R. Cammi, J. W. Ochterski, R. L. Martin, K. Morokuma, O. Farkas, J. B. Foresman and D. J. Fox, 2016.

64. G. te Velde, F. M. Bickelhaupt, E. J. Baerends, C. Fonseca Guerra, S. J. A. van Gisbergen, J. G. Snijders and T. Ziegler, *J. Comput. Chem.*, 2001, **22**, 931-967.
65. G. Schreckenbach and T. Ziegler, *J. Phys. Chem.*, 1995, **99**, 606-611.
66. E. D. Glendening, C. R. Landis and F. Weinhold, *J. Comput. Chem.*, 2013, **34**, 1429-1437.
67. J. Autschbach, *J. Chem. Phys.*, 2008, **128**, 164112.
68. C. A. O'Keefe, K. E. Johnston, K. Sutter, J. Autschbach, R. Gauvin, J. Trébosc, L. Delevoye, N. Popoff, M. Taoufik, K. Oudatchin and R. W. Schurko, *Inorg. Chem.*, 2014, **53**, 9581-9597.
69. A. J. Rossini, R. W. Mills, G. A. Briscoe, E. L. Norton, S. J. Geier, I. Hung, S. Zheng, J. Autschbach and R. W. Schurko, *J. Am. Chem. Soc.*, 2009, **131**, 3317-3330.
70. R. P. Young, C. R. Lewis, C. Yang, L. Wang, J. K. Harper and L. J. Mueller, *Magn. Reson. Chem.*, 2019, **57**, 211-223.
71. I. P. Gerothanassis and C. G. Tsanaktsidis, *Conc. Mag. Res.*, 1996, **8**, 63-74.
72. R. P. Young, B. G. Caulkins, D. Borchardt, D. N. Bulloch, C. K. Larive, M. F. Dunn and L. J. Mueller, *Angew. Chem., Int. Ed.*, 2016, **55**, 1350-1354.
73. J. Zhu and G. Wu, *J. Am. Chem. Soc.*, 2011, **133**, 920-932.
74. J. M. Aramini and H. J. Vogel, *J. Am. Chem. Soc.*, 1994, **116**, 1988-1993.
75. S. Gaemers, J. van Slageren, C. M. O'Connor, J. G. Vos, R. Hage and C. J. Elsevier, *Organometallics*, 1999, **18**, 5238-5244.